AGU
ADVANCING
EARTH AND
SPACE SCIENCE

JGR Planets

Key Points:
- Super high frequency events are a class of signals observed by the InSight seismometer on Mars
- Seven hundred and eighty events have been observed, typically lasting 20 s with energy mainly on horizontal components between 5 and 30 Hz
- Events appear in clusters and are likely associated with local thermal sources similar to observations on the Moon

Correspondence to:
N. L. Dahmen,
Email: nikolaj.dahmen@erdw.ethz.ch

Super High Frequency Events: A New Class of Events Recorded by the InSight Seismometers on Mars

Nikolaj L. Dahmen[1] [iD], **John F. Clinton[2]** [iD], **Savas Ceylan[1]** [iD], **Martin van Driel[1]** [iD], **Domenico Giardini[1]** [iD], **Amir Khan[1,3]** [iD], **Simon C. Stähler[1]** [iD], **Maren Böse[1,2]** [iD], **Constantinos Charalambous[4]** [iD], **Anna Horleston[5]** [iD], **Taichi Kawamura[6]** [iD], **Guenolé Orhand-Mainsant[7]**, **John-Robert Scholz[8]** [iD], **Fabian Euchner[1]** [iD], **William T. Pike[4]** [iD], **Renee C. Weber[9]**, **Philippe Lognonné[6,10]** [iD], and **William B. Banerdt[11]** [iD]

[1]Institute of Geophysics, ETH Zurich, Zurich, Switzerland, [2]Swiss Seismological Service, ETH Zurich, Zurich, Switzerland, [3]Institute of Theoretical Physics, University of Zurich, Zurich, Switzerland, [4]Department of Electrical and Electronic Engineering, Imperial College London, London, UK, [5]School of Earth Sciences, University of Bristol, Bristol, UK, [6]Université de Paris, Institut de physique du globe de Paris, CNRS, Paris, France, [7]Institut Supérieur de l'Aéronautique et de l'Espace SUPAERO, Toulouse, France, [8]Max Planck Institute for Solar System Research, Göttingen, Germany, [9]NASA Marshall Space Flight Center, Huntsville, AL, USA, [10]Institut Universitaire de France, Paris, France, [11]Jet Propulsion Laboratory, California Institute of Technology, Pasadena, CA, USA

Abstract We present a new class of seismic signals that are recorded by the seismometer placed on the surface of Mars as part of the NASA InSight mission. The signals, termed super high frequency (SF) events, are of short duration ($\sim$20 s), are often similar in amplitude, and feature high-frequency energy between $\sim$5 and 30 Hz that is dominant on the horizontal components. For detection and characterization of SF events, we employ the available continuous 20 samples per second (sps) data from the Very Broadband instrument. Due to bandwidth limitations, 100 sps data from the short-period sensor are only partially obtainable, but they aid in analysis of the frequency content above 10 Hz and in distinguishing the events from high-frequency noise. From June 2019 to May 2020, 780 SF events have been detected. The events observed occur in repeatable patterns that last for weeks. Initially, the SF events were clustered in the hours before sunset, but more recently, they have been distributed across the evening period. Based on template matching techniques, we have identified 16 distinct families that generally follow the temporal clusters. A thermal origin of these events is suggested, since the majority of the events fall within a $\pm$2 h time window around sunset with extreme temperature changes. The SF events have similarities with thermal events observed on the lunar surface from data collected during the Apollo missions.

Plain Language Summary The seismometers on Mars are recording high-frequency signals of short duration. Seven hundred and eighty of these events have been found so far, that can be categorized into families with comparable signal shape. Each family repeats for a limited number of days at similar times of the day. At first, they occurred at or shortly before sunset, but more recently they are being observed later in the Martian evening. We infer these signals originate from close to the lander but not the lander itself, and may be related to thermal cracking, like the lunar thermal events observed during the Apollo missions.

1. Introduction

The NASA InSight mission successfully landed on Mars on November 26, 2018 (defined as Sol 0, where sol is the Martian day corresponding to $\sim$24 h 40 min), in Elysium Planitia. On Sol 25, the lander placed the Seismic Experiment for Interior Structure (SEIS) on the Martian surface. SEIS includes a three-component Very Broadband (VBB) and a three-component Short Period (SP) seismometer (Lognonné et al., 2019). Since Sol 66, SEIS has been covered by the Wind and Thermal Shield (WTS) to minimize atmospheric effects. To complement the seismometer and as a means of characterizing atmospherically induced seismic noise, the Auxiliary Payload Sensor Suite records the surface pressure and also includes the Temperature and Winds for InSight sensors (TWINS) to measure the temperature, wind speed, and wind direction (Lognonné et al., 2019). A description of the initial geophysical observations of the mission can be found in Banerdt et al. (2020), while initial results on seismicity and interior structure are summarized in Giardini et al. (2020);

Lognonné et al. ([2020](#)). InSight is located within Homestead Hollow, a shallow sandy crater with a 20 m diameter, containing a few visible rocks. This setting and the local geology of the landing site are described in Golombek et al. ([2020a](#)); Golombek et al. ([2020b](#)).

The seismic data are routinely monitored by the Marsquake Service (MQS), a core mission service that is also tasked with curating the Martian seismicity catalog for the project (Clinton et al., [2018](#), [2020](#)). Since the source mechanisms of the various events cataloged by MQS are not unambiguously known, MQS has adopted a naming convention that distinguishes between event types in terms of the frequency content. The marsquakes observed so far are categorized chiefly into signals dominated by either long-period or high-frequency energy. To the former belong two groups of events, the *low frequency* and *broadband* (BB) events that are characterized by energy mainly below 2.4 Hz (only BB events have energy at or slightly above 2.4 Hz, Clinton et al. ([2020](#))). The high-frequency event family (van Driel et al., [2021](#)) includes energy at the 2.4 Hz mode, which is assumed to be a local resonance in the subsurface, and above that. Distinguished are the 2.4 Hz events, with excitations centered around 2.4 Hz; the *high frequency* (HF) events, with energy predominantly at 2.4 Hz and above; and the *very high frequency* (VF) events, a special case of the HF events with significantly more high-frequency energy (above 5 Hz), in particular on the horizontal components. For a detailed overview, we refer the reader to Clinton et al. ([2020](#)). The Martian dataset is complex to analyze, and in addition to the events cataloged by the MQS, a variety of nonseismic signals including effects of the atmosphere, operational activities and artifacts of the sensor are present in the data. These are summarized in Ceylan et al. ([2020](#)), together with the availability of the seismic and nonseismic channels during the mission.

In this study, we focus on the super high frequency (SF) events. The signals are clearly different to the other events cataloged by the MQS, as they do not include energy below 4 Hz, and by comparison are of very short duration (~20 s). Since the source of these events is currently unknown but is most likely very local, that is, in the immediate vicinity of the lander, as suggested by the short duration and high frequency content, MQS categorizes the events as other signals, separately from the high-frequency and low-frequency event families (Clinton et al., [2020](#)). We primarily use data from the VBB instrument (channels 02.BH[UVW]), that started to record data continuously with 20 samples per second (sps) from around Sol 190 (apart from the gap related to solar conjunction between Sols 268 and 288). Due to limitations of the bandwidth that is usable for data transmission to Earth, higher sampling rates of the SP sensor (channels 65.EH[UVW], sampled at 100 sps) are only requested for selected events.

In the following sections, we describe the characteristics of the SF events and compare them, among others, to the VF events. The detection methods and the temporal distributions of all events discovered in the period Sol 190–522 are presented. We investigate the similarity of the waveforms using cross-correlation techniques, and based on that, group the events into families. Finally, we discuss potential origins. Comparing the SF events to a particular set of signals that were observed in the Apollo lunar seismic data set and that are believed to be thermally generated, we entertain the possibility that SF events are similarly of thermal origin.

2. Characteristics of SF Events

In the following, we modify the MQS naming convention and label SF events as *Tssssa*, (where *ssss* indicates the sol on which the event occurred, and *a* distinguishes between multiple events on that sol; all other event classes are named as *Ssssssa*). Spectrogram and 5–9 Hz band-passed time series for event *T0190a* are shown in Figure [1](#) using the SP sensor (channels 65.EH[UVW]) output in velocity, after the gain removal and rotation to the vertical-north-east (ZNE) coordinate system.

In stark contrast to all the other event types MQS is cataloging, the observed signals for SF events have a very short duration of about 20 s and do not exhibit distinct phases. The frequency content of the signal can range from 5 to 30 Hz, although most events are restricted to a narrower bandwidth (7–9 Hz). For all observed events, energy is strongest on the horizontal components and is almost absent on the vertical component. Generally, there is no excitation of any of the many known modes associated with the lander, SEIS, and the semi-rigid cable connecting the two, called tether, though all three components show excitation of the broad high-frequency mode around 28 Hz. T0190a is a high-amplitude SF event relative to what is gen-
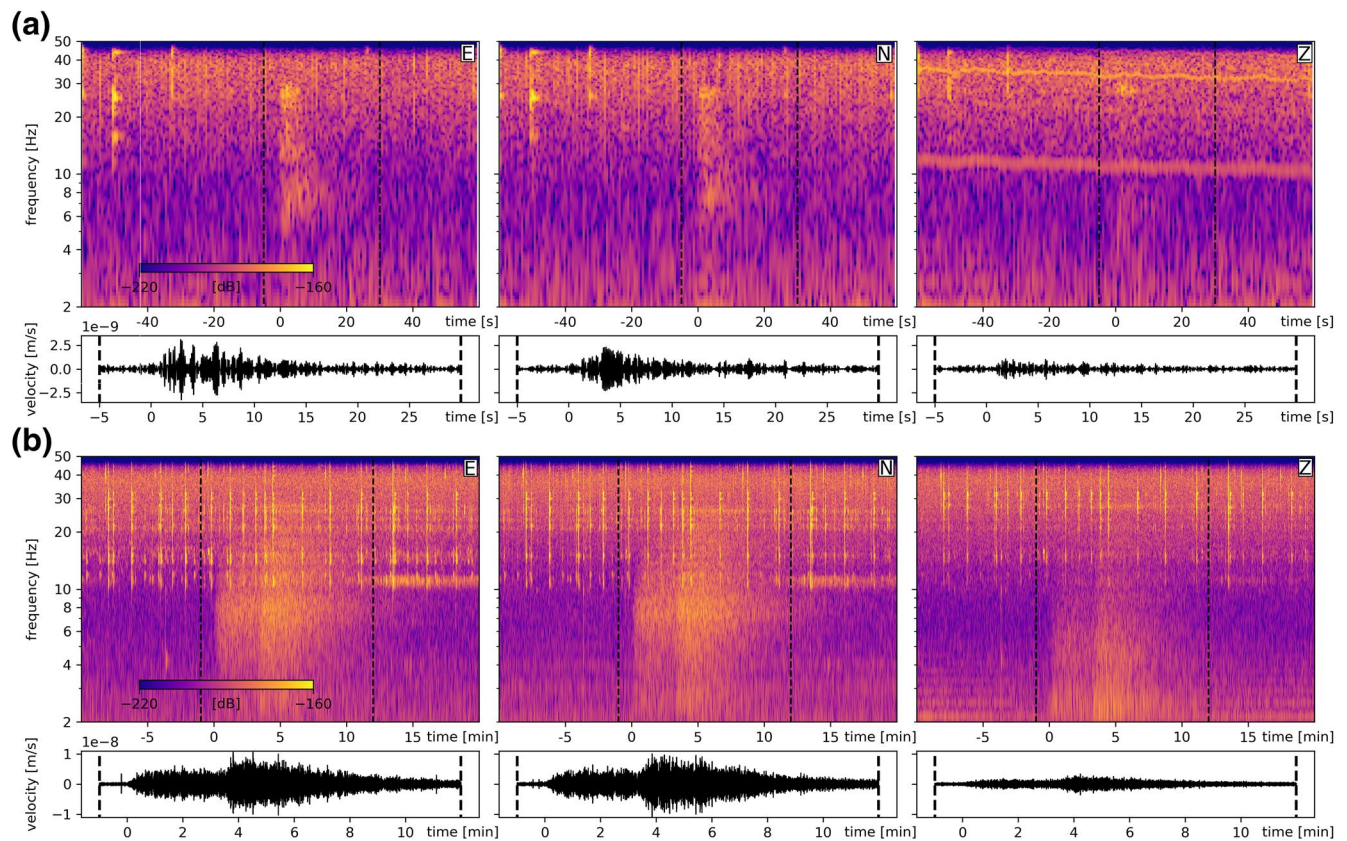
Figure 1. Comparison of SF and VF events: (a) SF event *T0190a* (high amplitude) on Sol 190, 17:31 LMST—spectrogram (power spectral density) shows 120 s time window with the event start aligned on ~0 s. The vertical black-dotted lines indicate the time period of the waveforms below, given in a 5–9 Hz bandpass and with the same scale on all components. (b) VF event *S0334a* on Sol 334, 18:51 LMST—spectrogram of 30 min time window is displayed, a zoom-in of the 5–9 Hz bandpass of the waveforms is given below. LMST, Local Mean Solar Time; SF, Super high frequency; VF, very high frequency.

erally observed. The smaller SF events are only marginally above background noise and therefore are only barely visible in the spectrogram and time series. An example is shown in the Figure A3b.

In general, analysis of the frequency content above 10 Hz is restricted to events for which 100 sps data are available. The high frequencies can be difficult to interpret as the bandwidth is often contaminated by repetitive patterns of so-called donks. The noise-related donks are very short duration (a few seconds) impulsive signals that strongly excite lander modes above 10 Hz (Ceylan et al., 2020). Compaire et al. (2020) analyzed the occurrence of donks during the evening hours from 17:00 to 22:00 Local Mean Solar Time (LMST) for Sol 180–261. The mean time delay between two consecutive donks was found to be around 45 s or less, with the shortest mean delay of ~10 s during the peak hour between 17:00 and 18:00 LMST, where they occurred most frequently. Figure A3e shows an example where donks are taking place even more often. Consequently, donks are basically present at all times and are often overlapping SF events. Additionally, there are long-period transient signals (usually below 1 Hz) in the data, that appear as one-sided pulses in the raw waveform. Termed as glitches, it is understood that these signal are a result of temperature-related stress relaxation inside SEIS and from the lander (Scholz et al., 2020).

Despite the very short duration of SF events, they are distinct from lander- and SEIS-induced signals, in particular because they do not excite the many lander modes and share key features with VF events. For comparison, a VF event (S0334a) is shown in Figure 1b. S0334a has a duration of around 10 min and shows a clear primary and secondary phase arrival. Several spikes are visible in the waveforms (most notable on the east component), that correspond to donks extending below 9 Hz. The dominant frequency content and the difference between horizontal and vertical energy is very similar to that of the SF events. Also, the excitation of the ~28 Hz mode is present on all components.

3. Detection and Temporal Distribution of Events

Although SF events prior to Sol 190 have been seen, we commence our investigation on Sol 190 (June 9, 2019), the date when continuous 20 sps data from the VBB sensor (channels 02.BH[UVW]) became available, and continue up until Sol 522 (May 17, 2020). The first observed SF event, and currently the earliest event included in the MQS catalog, occurred on Sol 45, 17:48 LMST, and was detected by the SP sensor on the Martian surface, but before the WTS was placed over SEIS. From a practical point of view, and like all other type of events, SF events were first recognized through manual review (Clinton et al., 2020). However, SF events are difficult to systematically catalog, because of (1) their short duration; (2) lack of energy on the vertical component (on which all other event types are detected); and (3) absence of amplification of the 2.4 Hz mode that is a key feature of most other events. Yet, these signals are the only event types so far that lend themselves to automated detection.

Systematic detection uses the fact that for all SF events, most of the energy is found on the horizontal components in the 7–9 Hz frequency range with no energy below 5 Hz. We selected this bandwidth carefully so as to avoid presence of wind-induced lander modes. Also, the frequent transient, short-duration signals like donks or glitches do not (or only rarely) excite this bandwidth (Ceylan et al., 2020). A particularly large amplitude lander mode occurs at 4 Hz, that appears to be strongly excited by wind (wind also excites broadband seismic noise within the 7–9 Hz window). Our detection algorithm takes the ratio of energy in the frequency bands 7–9 Hz and 3–5 Hz to find SF events. A positive detection is obtained when the ratio on at least one of the horizontal components exceeds a defined threshold. False detections are manually removed by visual inspection of the spectrogram. More details on the detection are given in the Figure A1. This approach was validated by comparing the results with an SF catalog found by manual data review covering a 2-month period. The detection threshold was chosen so that all manually identified events were identified with this approach. We use the VBB sensor output in velocity following the overall gain removal and rotation to ZNE. Although SF events are equally visible in 20 sps VBB and SP recordings, the VBB sensor is preferred over the SP sensor (67.SH[UVW]) due to the completeness of the data set (data availability is shown in Figure 2 of Ceylan et al., 2020).

Since the ratio-based detector works best if there is low wind excitation, small-to-moderate amplitude SF events may not be identified if these occur during a windy period. Because the majority of SF events fall into a small number of clusters defined by similar waveforms (see Section 4), a template matching approach (Bulow et al., 2005; Gibbons & Ringdal, 2006) is used to complete the catalog. To obtain a template with high signal-to-noise ratio, waveforms of similar events are stacked. This stacked template is then cross-correlated with the continuous data to detect new events, as a result of which the catalog is extended with additional events that occur during the noisier times of the day (for more details, see Figure A1). In this manner, we detected 780 events, 581 of these were found with the ratio-based detector and an additional 199 using template matching. Time of occurrence and number of events per sol are shown in Figure 2.

To provide an overview of the daily noise pattern on Mars relevant to the SF events, the background of the figure is formed by averaging the spectrograms in the 7–9 Hz band-pass of the VBB east component. Resulting from the influences of the local weather, we observe a division of the Martian day into three major parts: a noisy night (3–4 h after sunset to 1 h after sunrise), a high-noise day (1 h after sunrise to 1–2 h before sunset), and a relative quiet evening (1–2 h before sunset to 3–4 h after sunset), matching the broadband pattern. The noise pattern is changing with the seasons on Mars. During the more recent sols, the aforementioned trisection of the Martian day is disappearing, giving way to high-noise periods throughout most of the day. A more detailed description of the noise patterns, including full broadband information can be found in Ceylan et al. (2020) and Giardini et al. (2020), while analysis of the atmospheric conditions has been considered in more detail by Banfield et al. (2020).

Constrained by the noise pattern and comparable to most other events in the MQS catalog, SF events are primarily detected during quiet periods from just before sunset to shortly before midnight. During this time window, SF events are not randomly distributed, but are mainly confined to clusters at similar times of the day that repeat for a number of sols. Because of their relatively low amplitudes, SF events are not detected during the high-noise period of the day. Only very recently, as short low-noise windows open up during the day, we spotted a handful of events occurring during the day (not included in the overview, an example can be found in the Figure A6). The amplitude of the events are indicated, in terms
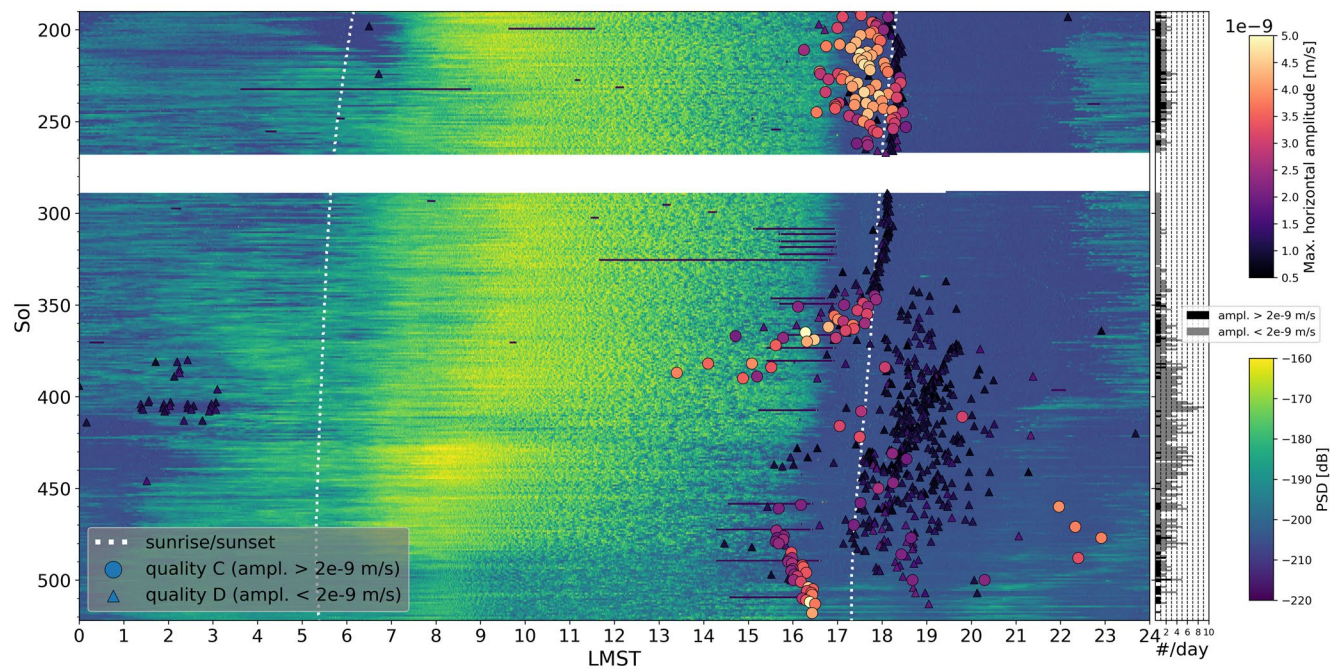
Figure 2. Temporal distribution of detected SF events with maximum amplitude [m/s] and quality (C or D, as in MQS catalog). The panel on the right side counts the events per day, the background shows the power spectral density (PSD) of the 7–9 Hz bandpass of VBB's east component (channel 02.BHE). No data are available during the solar conjunction (∼Sol 268–288). LMST, Local Mean Solar Time; MQS, Marsquake Service; SF, Super high frequency; VBB, Very Broadband.

of the maximum horizontal amplitude (Euclidean-norm of E-N components) in the 7–9 Hz band-pass in Figure 2. Within this narrow band-pass, the events fall within a single order of magnitude between 5×10^{-10} and 5×10^{-9} m/s. Detections are separated into 158 high- and 622 low-amplitude events, based on the threshold of 2×10^{-9} m/s. In the MQS catalog, the high-amplitude events are assigned quality C, while the low-amplitude events are quality D. In contrast to the high-amplitude events, the low-amplitude events do not seem to consistently excite the very high frequencies (>10 Hz, see Figures A3–A5).

High-amplitude events are primarily observed during three distinct periods, namely between Sol 190–267 (Sol 268 marks beginning of solar conjunction), Sol 345–375, and Sol 460–520. During the first two periods, the events fall largely within a 1–2 h time window from shortly before to just after sunset. During the third period, the events form highly repetitive patterns, with events occurring around 16:00 LMST, between 18:00–19:00 LMST, and to a lesser extent between 22:00–24:00 LMST. There are several examples of multiple high-amplitude events on one single sol (e.g., three on Sol 477). Within each of the temporal clusters, a gradual change of the maximum amplitude over time is visible. Looking at the low-amplitude events, we observe about one event per day during Sol 190–350 (except during solar conjunction), that follows sunset remarkably closely, but abruptly stops. Following this, the number of events per day increases significantly with occurrence time becoming more widespread. Most events fall within a 2–3 h period after sunset. From about Sol 470 onwards, the number of events per day decreases again with a concomitant increase in the background noise level. Finally, an exceptional increase in the number of low-amplitude events in the early morning during several unusually quiet hours between Sol 380–390 and Sol 400–410 are observed.

4. Similarity of Waveforms

We discovered very similar waveforms across a large number of events and have classified them into families. For the grouping, representative events or stacks of events (templates) of the individual temporal cluster are identified and then compared to all other events. More precisely, the time series of each template is
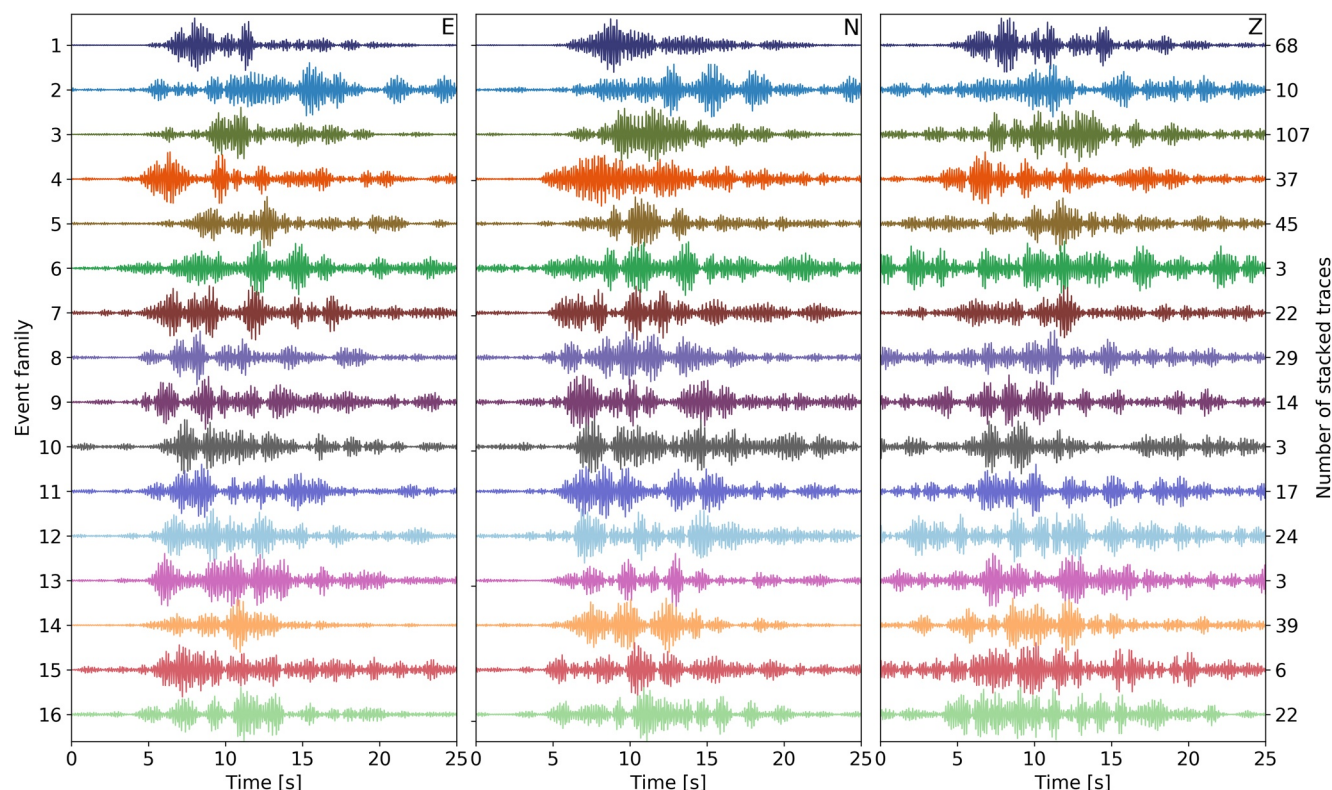
Figure 3. Stacked and normalized waveforms (7–9 Hz) of the 16 event families. The event family and the number of the stacked traces are shown on the vertical axis on the left and right side, respectively. The color scheme is consistent with the following figures.

filtered in the 7–9 Hz band-pass, and then cross-correlated with the waveforms of all detected events. When the correlation coefficient of the horizontal components exceeds a defined threshold, the events are included into the template family. This step is repeated with the stacked waveforms of all previously found event families. From this procedure, we identify 16 different families that contain the majority of the high-amplitude events and various striking low-amplitude events. The associated stacked, 7–9 Hz band-pass-filtered, waveforms of each family are shown in Figure 3. Due to the low signal strength on the vertical component and the varying number of added traces, stacking does not always produce a clear waveform.

Figure 4 displays the temporal distribution of the 16 families as well as events that are not assigned to any particular family. The observed temporal clusters generally separate into discrete families of comparable waveforms. The characteristic signals of each family is only recorded for a limited duration and, once they initially stop, they do not recur later in the same form. However, some event families seem to be similar to each other. To investigate this, we compute a similarity matrix of all classified events, which is shown in Figure 5. The values are based on the mean horizontal cross-correlation values of time series of 25 s duration, filtered between 7 and 9 Hz. The events are ordered first by family and then by date.

The families are generally easily distinguishable, but there are also similarities between several of them, most obviously between families 1 and 4. Family 1 contains the majority of the high-amplitude events during Sol 190–267 and their similarity values show a gradual change over time, that correlates with the increase and decrease of the event amplitudes (see Figure 2). The events at the end of the cluster seem to resemble family 4, which is also indicated by similarity of the stacked waveforms. The gradual change over time is also visible for family 3, that indicates a division of the events happening before and after solar conjunction. Event family 7, which occurs mostly during the early morning, appears to be most different from all others (also visible in the spectrogram in Figure A4a). The similarity value of the remaining unclassified events suggest that most could be assigned to one of the existing families, yet they fall below the defined threshold (all events are given in Figure A2).
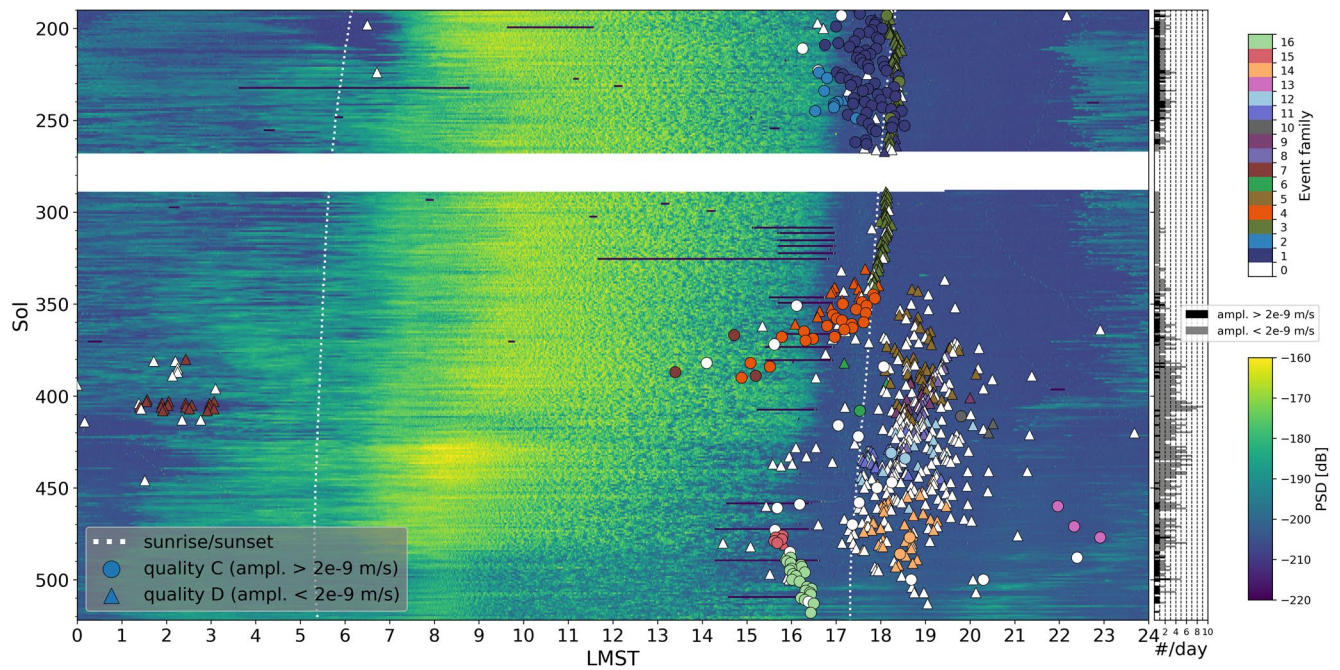
Figure 4. Occurrence of the 16 event families and unassigned events (white). The background shows the power spectral density (PSD) of the 7–9 Hz bandpass of VBB's north component (channel 02.BHN). LMST, Local Mean Solar Time; VBB, Very Broadband.
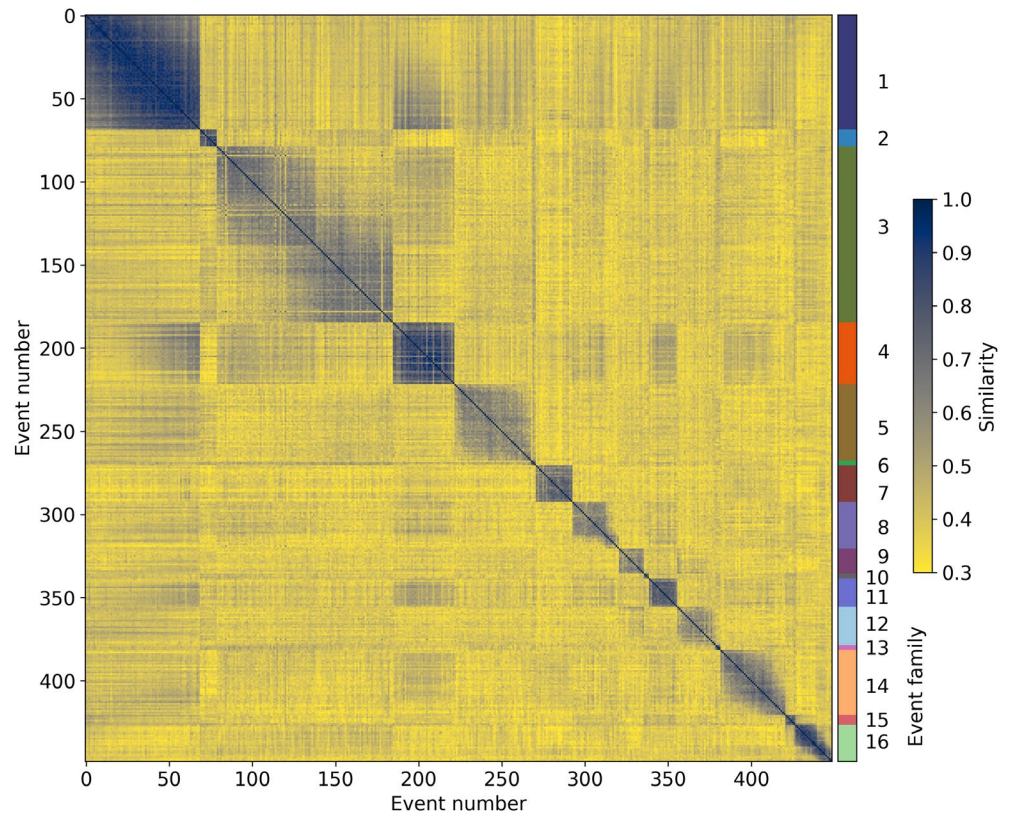

Figure 5. Similarity matrix of all categorized events. The events are ordered first by family and then by date. The given similarity values correspond to the mean horizontal cross-correlation values of 25 s long waveforms in the 7–9 Hz bandpass. Right sidebar shows the event family.

5. Discussion

The SF events encompass short-duration signals with significant frequency content in the 7–9 Hz band-pass (and often above that) and are found to be unrelated to lander modes, donks, or glitches. The fact that SF events can be subclassified into different families with similar waveforms suggests a limited number of distinct sources that repeat for several weeks at similar times of the day.

Compared to the high-noise level during the day, the amplitudes of the SF events are low and are not detected during that period. In the first half of the analyzed period (Sol 190–350), the vast majority of SF events fall within a short time window around sunset, while almost no events are detected in the similarly quiet late-evening period. In view of the fact that event family 3 appears to closely follow sunset, a possible correlation with the diurnal temperature cycle is suggested in analogy with the Moon.

Analysis of the Apollo lunar seismic data revealed a set of repetitive short-duration (∼1–5 min), high-frequency signals, whose occurrence times correlated strongly with lunar sunrise and sunset (Bulow et al., 2005; Duennebier, 1976; Duennebier & Sutton, 1974; Dimech et al., 2017; Lammlein et al., 1974; Larose et al., 2005; Sens-Schönfelder & Larose, 2010). These events, labeled thermal moonquakes, showed a number of characteristics partly reminiscent of the Martian SF events: (1) they were periodically recurring; (2) had similar waveforms; (3) lacked distinct phase arrivals; (4) were of comparable amplitudes; and (5) had emergent onsets, long rise times, followed by long signal decay. Duennebier and Sutton (1974) also identified another class of signals distinguished by a shorter rise time, a shorter duration (∼1 min) and distinct spectral peaks related to the lunar module (Latham et al., 1970), but like the thermal moonquakes, they clustered around sunrise and sunset. These signals were not investigated further, yet it was suggested they likely originated from thermal adjustments within the lunar module.

With the deployment of the geophone array as part of the Apollo 17 seismic profiling experiment (Cooper et al., 1974; Kovach & Watkins, 1973), thermal moonquake sources could be associated to nearby craters (within ∼300 m) and boulders (within meters). As a possible source mechanism, Duennebier (1976) suggested thermally driven movement and cracking of regolith within craters, rocks and boulders. In a more recent study, Dimech et al. (2017) classified potential thermal moonquakes based on their waveform into impulsive, intermediate, and emergent event types. In Figure 6, we show spectrograms and waveforms of the aforementioned three types of events recorded at geophone 1 at a distance of ∼148 m distance from the lunar module (velocity sensor with usable frequency range between 3 and 30 Hz and sampled at ∼118 sps (Kovach & Watkins, 1973; Sens-Schönfelder & Larose, 2010)).

The impulsive event type has a short duration of about 1 min, and high-frequency energy exceeding 30 Hz. Additionally, spectral peaks at ∼4 and ∼10 Hz are visible, suggesting that the signal originates from the lander. The emergent (and intermediate) event type does not show any clear spectral peaks, lasts longer (more than 5 min), and the frequency content is restricted to lower frequencies (up to 10–20 Hz). Since the geophones only recorded vertical ground motion, a more detailed comparison with the SF events, where most of the energy is contained on the horizontal components, is complicated. In terms of signal duration, the impulsive event type comes closest, but the SF events do not show any distinct spectral peaks that would indicate the lander as a source.

Using merged 3D images from the Mars Exploration Spirit Rover, Eppes et al. (2015) demonstrated that the preferred directional cracking of Martian boulders can be related to the diurnal patterns of solar-induced stresses. Several smaller craters and rocks were found in the vicinity of the InSight lander, that could be prone to thermal degradation (Golombek et al., 2020a, 2020b). The amplitudes of the diurnal temperature variations on Mars are smaller in comparison to the Moon, yet, they are still on the order of 100 K and thermally induced cracking can be expected.

The atmospheric temperatures at the InSight landing site are measured by the two TWINS booms. The sensors are situated on top of the lander (∼20 cm above deck Golombek et al., 2020 and ∼1.2 m above ground) and are consequently disturbed by the effect of the lander deck and its solar panels, and also by their nonnegligible radiative cross-section (Banfield et al., 2020). Figure 7 summarize (a) the atmospheric temperatures measurements of sensor 1 (channels 10.LKO, 10.VKO, 13.LKO) and (b) its rate of change during the period Sol 190–522, which is the same period used for SF analysis in this study (equivalent plots for sensor 2 are shown in Figure A7). The occurrence of the 780 SF events identified in this study are overlain. We observe
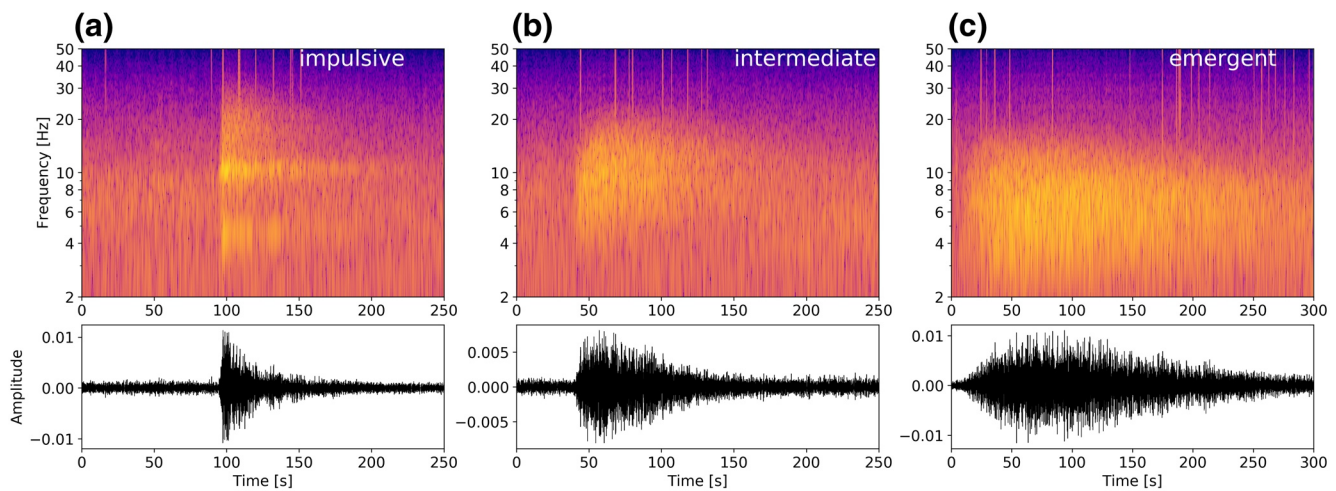
Figure 6. Local and high-frequency events from the moon: (a) impulsive (August 30, 1976 14:53), (b) intermediate (August 15, 1976 13:01) and (c) emergent (August 31, 1976 00:03) events recorded by geophone 1 during the Apollo 17 seismic profiling experiment. The amplitudes are given in raw units, after preprocessing (despiking and bandpass filter).

rapid changes and note a striking short-duration increase of the temperatures just before sunset (also visible in the daily temperature profile, see Figure A8f), that was also observed in earlier missions, for example, by Mars Pathfinder (Schofield et al., 1997). The two TWINS sensors show large differences of up to ~25 K at a given time of the day, with higher values at sensor 1 (located to the East, toward sunrise) in the morning, and vice versa for sensor 2 (located toward the West, toward sunset) in the afternoon (see difference of both sensors in Figure 7c). In the first half of the period investigated, SF events fall within a time period of extreme temperature changes (or shortly after). The seasonal shift toward warmer evenings roughly fits the pattern of later-appearing events after Sol 350. Generally, it is observed that the high-amplitude events take place at higher temperatures and larger cooling rates relative to the low-amplitude events (see statistics in Figure A8).

However, we do not see any conclusive correlation of the atmospheric temperatures and the clustering of the SF events. Surely, the TWINS observations can only provide an approximate measure of temperatures at other points in the vicinity of the lander. The actual temperatures within various components of the lander, rocks or the regolith will deviate significantly due to local depths of insulating material and also to radiation and shadowing effects. In particular, since different SF clusters slowly vary in terms of event occurrence and amplitude for the weeks they are observed (if we assume these events are produced by cracking of different rocks), a promising lead would be to investigate the angle of the sun and the shadowed area cast by the lander and the instruments, both on a diurnal and a seasonal scale. This may give a better understanding of potential thermal relationships. Lastly, Figure 7d shows the temperature observed at SEIS under the WTS (02.VKI, 03.VKI), which is designed to have a thermal time constant on the order of 7 h (Mimoun et al., 2017). The increasing number of events after Sol 350 correlates with the higher temperatures under the WTS, due to the sustained higher daytime temperatures. But, similarly to the atmospheric temperatures, the beginning and ceasing of the clusters show no clear correlation. Further, the SF events were already observed prior to the deployment of the WTS on Sol 66 (Ceylan et al., 2020), for example, on Sol 45, 17:48 LMST. The correlation of event occurrence and high temperatures inside SEIS suggests that cracking is taking place inside a source that has a similar thermal constant as the WTS. Seasonally variations of insolation and shadowing on the source could then lead to delimited event clusters.

Another plausible explanation for these events is that they are associated with the lander, though seismic recording of thermal expansions is regularly recorded via donks and glitches that produce far more impulsive signals. The high-frequency donks also excite a range of different natural modes of the lander. In contrast, the SF events do not excite any known lander modes. A broad excitation between 25 and 30 Hz is routinely excited by the SF events that include energy this high, though the source of this mode remains unclear. It is notable that these SF events share a very similar frequency profile with the VF events that are located in regional epicentral distances from the lander (up to ~35°), and are thought to be shallow marsquakes (van Driel et al., 2021).
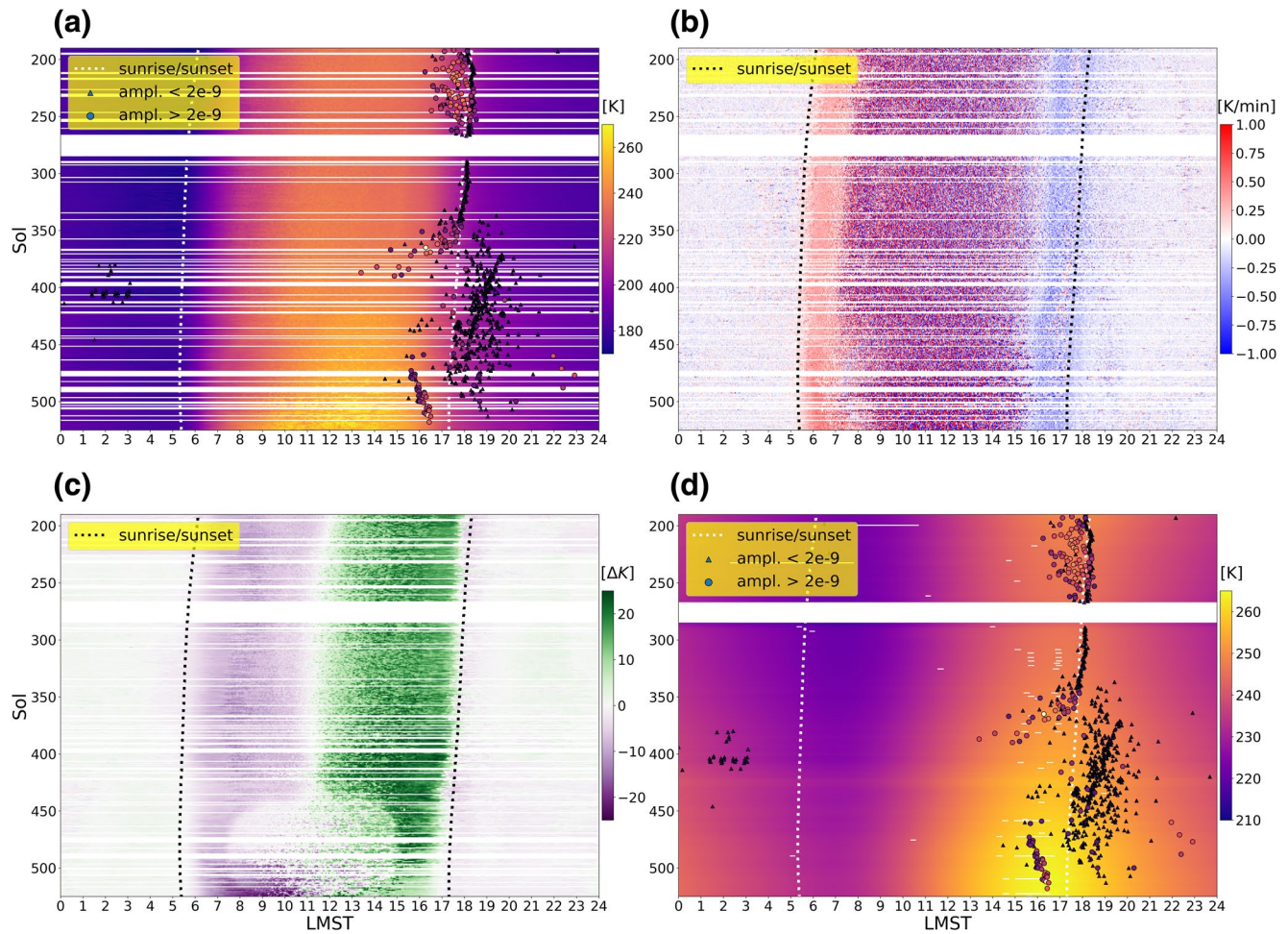
Figure 7. SF events and temperature from Sol 190 to 522: (a) atmospheric temperature - sensor 1, (b) its rate of change per minute, (c) difference of the atmospheric temperature sensors 1 and 2 and (d) scientific temperature under WTS. Data gaps are marked in white. LMST, Local Mean Solar Time; SF, super high frequency; WTS, Wind and Thermal Shield.

6. Conclusion

We described the characteristics of the SF events and showed the temporal distribution of the detected signals. Due to their relatively low amplitude, the detection is mainly restricted to periods with low-to moderate noise levels. Based on waveform similarity, the events were summarized into families that each recurred for only a limited number of weeks. The periodical recurrence of the events indicates a coupling to the diurnal temperature cycle, by analogy to signals observed on the Moon. We compared the events to thermal moonquakes and signals originating from thermal adjustments of the lunar lander, and investigated possible correlation with the atmospheric temperatures. However, at this stage, the source mechanism for the SF events still remains open. The extremely short duration, the lack of longer period energy, and the occurrence of the majority of events within hours either side of sunset, suggests the source is local and associated with thermal cracking. Since the events do not excite lander modes routinely excited by winds, we suggest the events are not associated with the lander. One possible explanation is these events are associated with thermal cracking within the local regolith or associated with surface rocks. A possible next step would be to estimate the required size of the source to produce the observed signals, and try to understand whether their duration is caused by scattering effects along the path or by reverberations of the source. However, we cannot fully exclude thermal adjustments of parts of the lander or instrumentation, nor other nonthermal mechanisms as a possible source. As we continue to collect more events moving through the seasons, we expect we will be able to better constrain the source of these intriguing Martian signals.
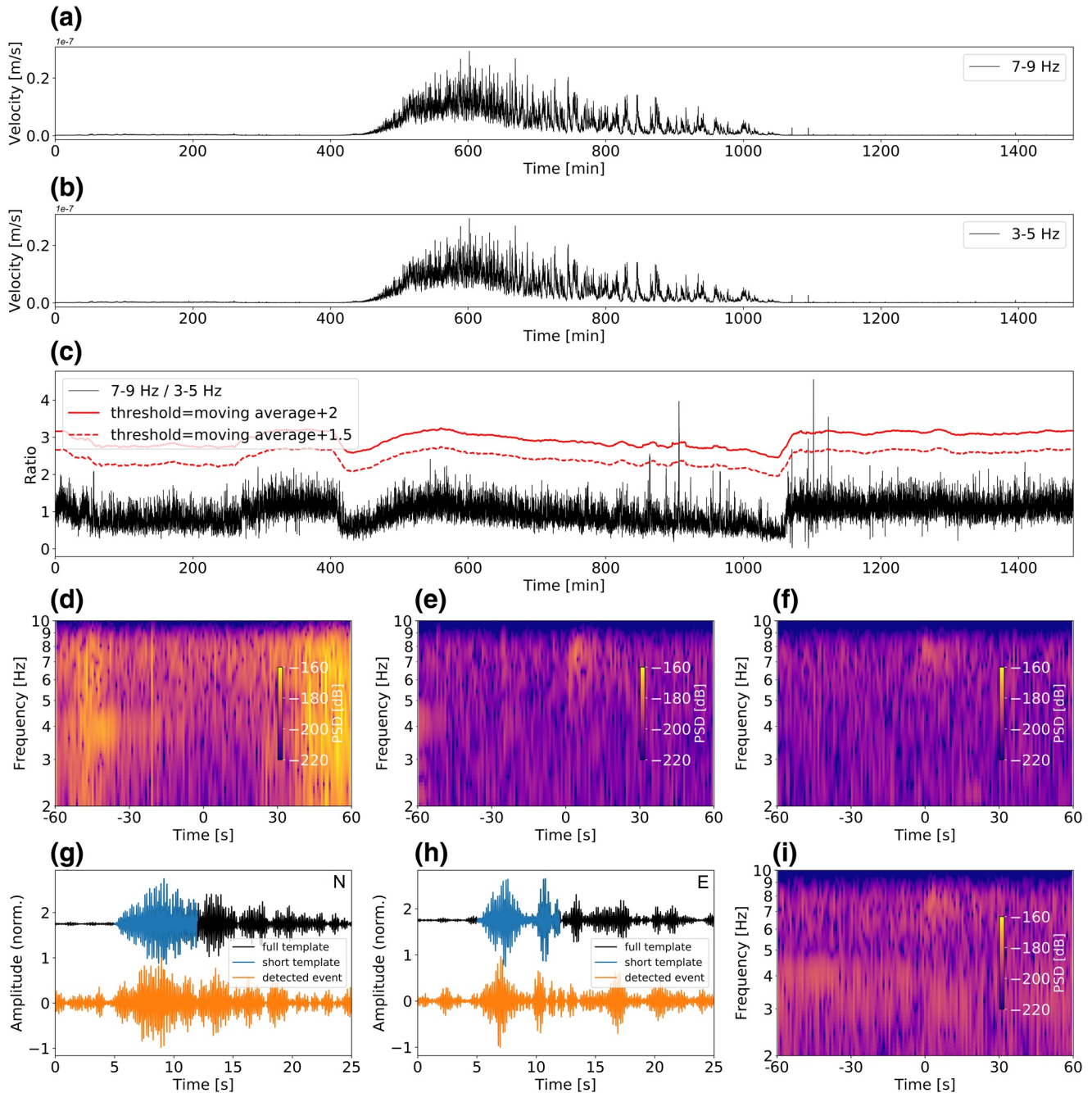
Appendix A

Figure A1. Detection of SF events on 20 sps VBB data: 7–9 Hz/3–5 Hz ratio approach for full Sol 195 (only north component shown)—(a) absolute value of velocity in 7–9 Hz bandpass, (b) absolute value of velocity in 3–5 Hz bandpass, (c) ratio of both bandpasses after applying a 5 s smoother, detection are made when the ratio surpasses the threshold, which is given by a 20 s moving average of the ratio plus a value of 2 (high threshold) or 1.5 (low threshold). Here, the three detections with the higher threshold are found to be (d) one false detection during noisy day period, (e) event T0195a, 17:52 LMST and (f) event T0195b, 18:13 LMST (all three spectrograms showing the north component). This method is applied on both horizontal components separately. With the lower detection threshold, additional very low-amplitude events are occasionally found, while the number of false detection increases significantly. In the template matching approach, stacked and normalized templates (7–9 Hz) of the 16 found event families are used. In (g) and (h), the north and east component of the full template (black) of event family 4 is given. For the detection, only a shorter, 7 s, template (blue) is used, that includes the main arriving energy. As an example of a successful detection, the waveforms of the event T0343a (orange) are added. All detections on the VBB data (7–9 Hz) with a cross-correlation value of >0.8 (mean value of both horizontal components) are checked to find missed events, for example, (i) event T0343a (north component), 16:55 LMST with a cross-correlation value of 0.95, that was not detected before due to the higher background noise level. LMST, Local Mean Solar Time; SF, super high frequency; VBB, Very Broadband.
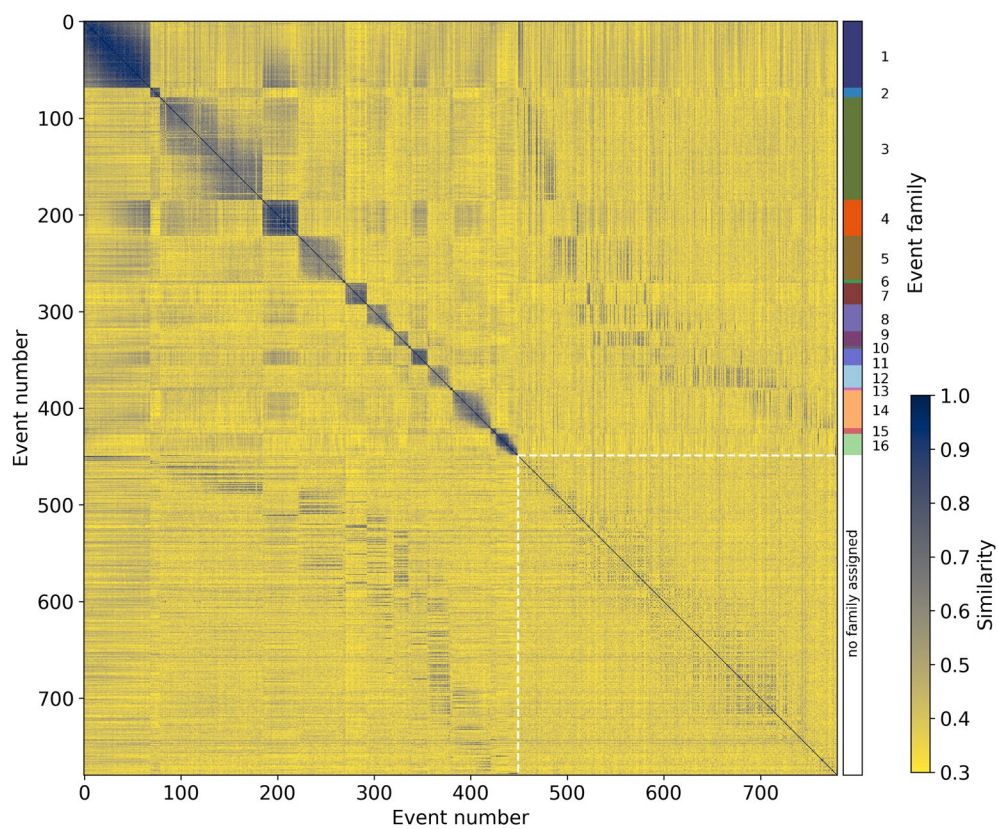
Figure A2. Similarity matrix of all events. The events are ordered first by family and then by date, the unassigned events are separated by the white-dotted lines and are ordered by date. The given similarity values correspond to the mean horizontal cross-correlation values of 25 s long waveforms in the 7–9 Hz bandpass. Right sidebar indicates the event family.
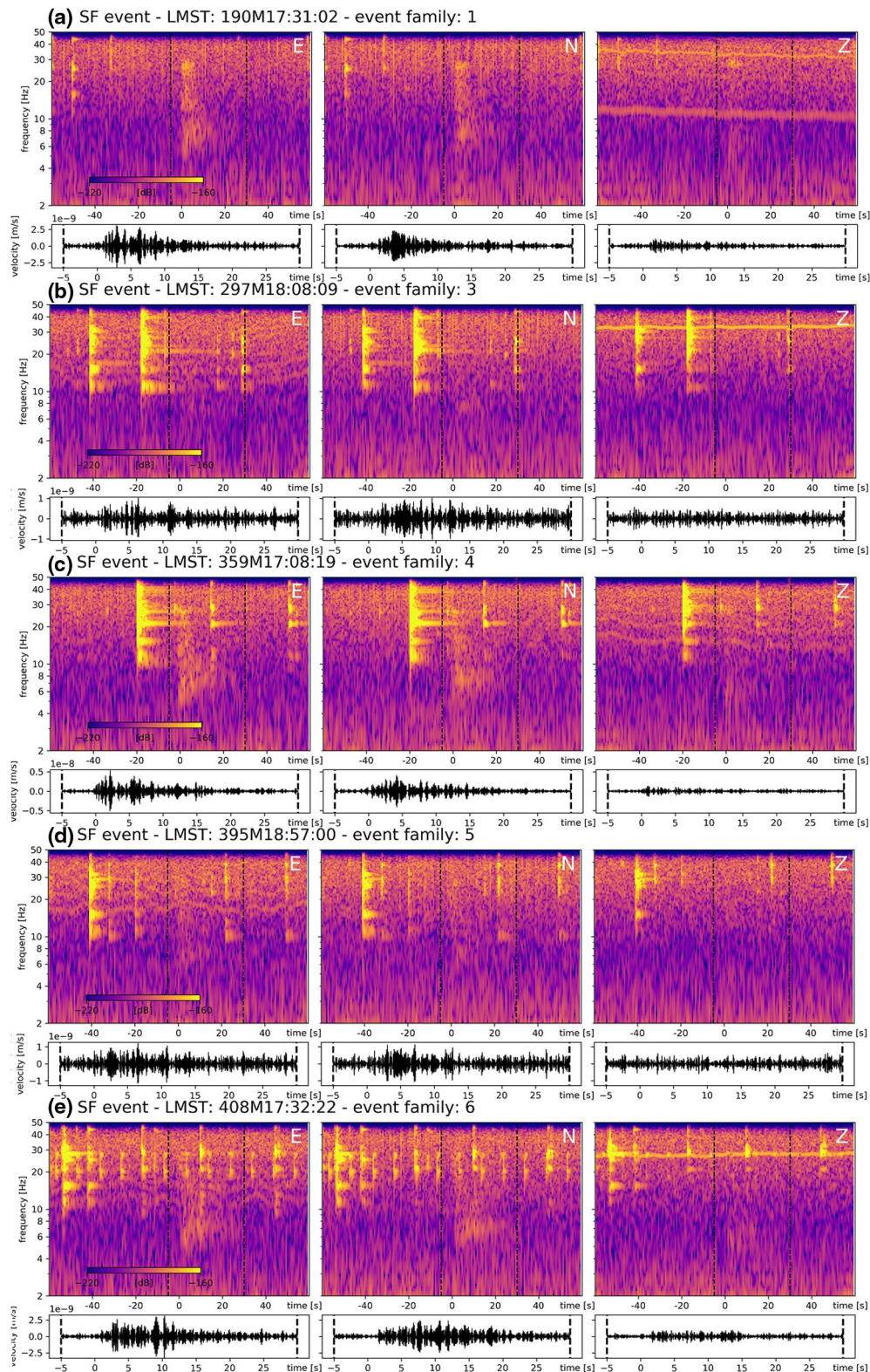
Figure A3. Spectrograms and waveforms (SP sensor) of SF events from family (a) 1 (*T0190a*), (b) 3 (*T0297a*), (c) 4 (*T0359a*), (d) 5 (*T0395b*), and (e) 6 (*T0408c*), no 100 sps data available for family 2, with the start time aligned on ~0 s. The vertical black-dotted lines in the spectrograms indicate the time period of the waveforms below, given in a 5–9 Hz bandpass and with the same scale on all components. Shown are examples with minimum contamination of donks (few second long, impulsive and high-amplitude signals that excite characteristic modes). LMST, Local Mean Solar Time; SF, super high frequency; SP, Short Period.
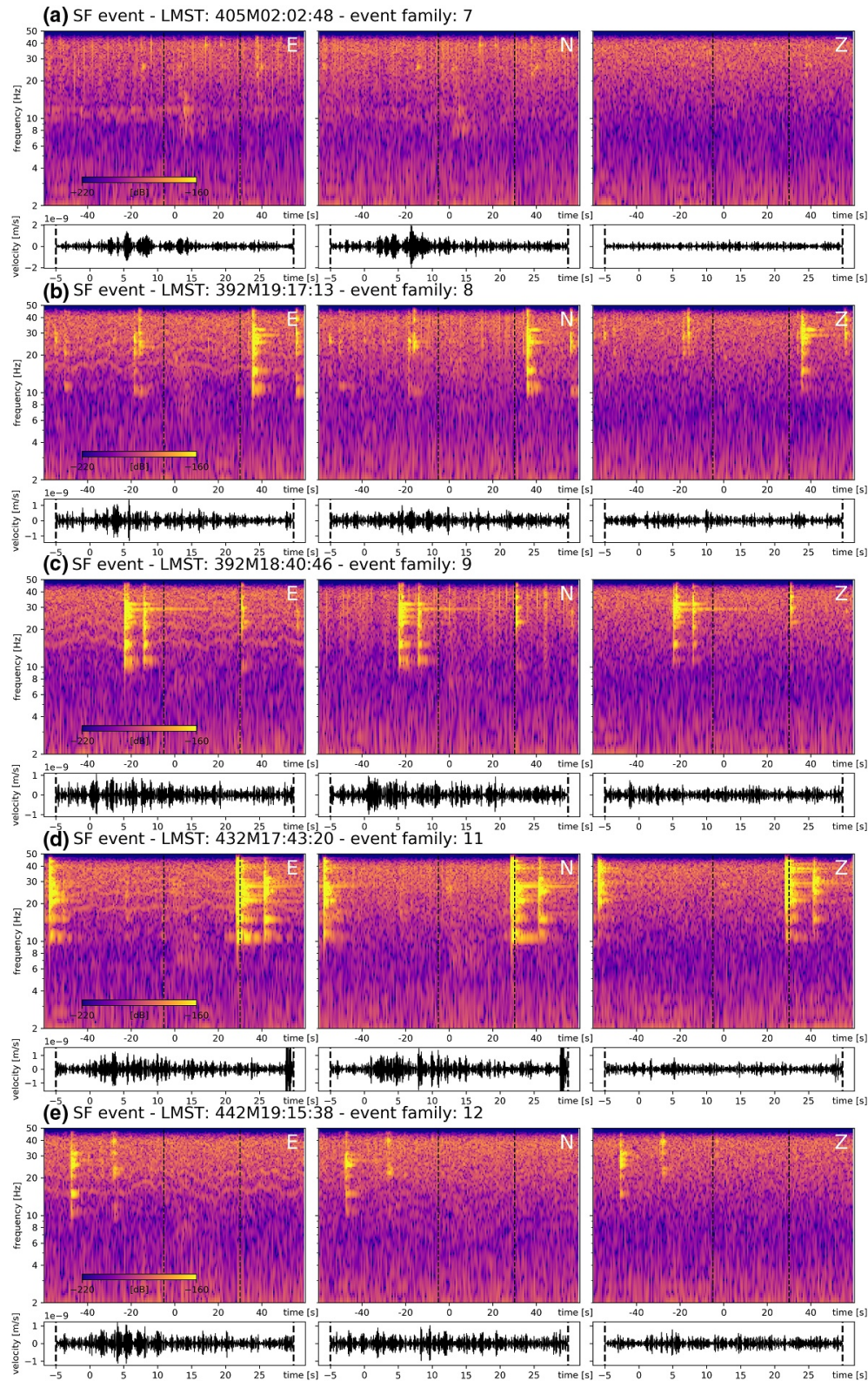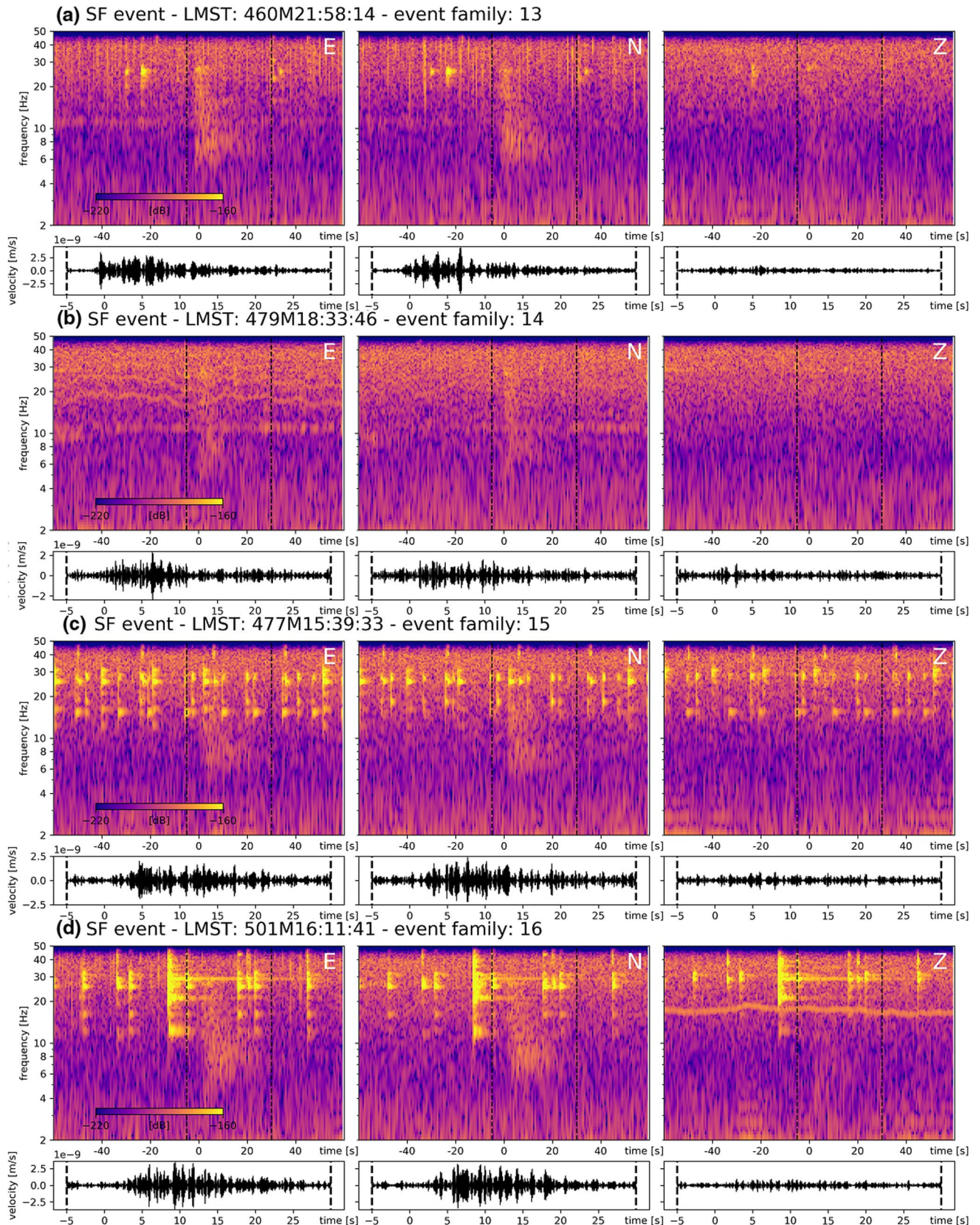
Figure A4. Spectrograms and waveforms (SP sensor) of SF events from family (a) 7 (*T0405a*), (b) 8 (*T0392d*), (c) 9 (*T0392b*), (d) 11 (*T0432b*), and (e) 12 (*T0442f*), no 100 sps data available for family 10, with the start times aligned on ~0 s. The vertical black-dotted lines in the spectrograms indicate the time period of the waveforms below, given in a 5–9 Hz bandpass and with the same scale on all components. Shown are examples with minimum contamination of donks. LMST, Local Mean Solar Time; SF, super high frequency; SP, Short Period.
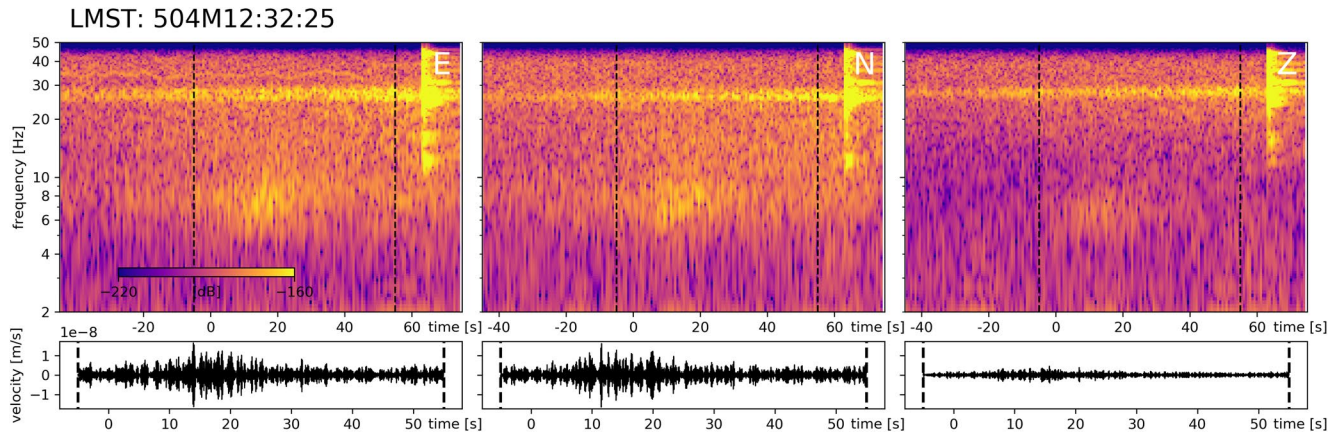
(a) SF event - LMST: 460M21:58:14 - event family: 13

(b) SF event - LMST: 479M18:33:46 - event family: 14

(c) SF event - LMST: 477M15:39:33 - event family: 15

(d) SF event - LMST: 501M16:11:41 - event family: 16

Figure A6. Spectrograms and waveforms (SP sensor) of potential SF event on Sol 504, 12:32 LMST with the start times aligned on ~0 s, detected during a short quiet window during the noisy day. This potential event differs from all other shown events in terms of a larger amplitude and longer duration. The vertical black-dotted lines in the spectrograms indicate the time period of the waveforms below, given in a 5–9 Hz bandpass and with the same scale on all components. LMST, Local Mean Solar Time; SF, super high frequency; SP, Short Period.

Figure A5. Spectrograms and waveforms (SP sensor) of SF events from family (a) 13 (*T0460d*), (b) 14 (*T0479c*), (c) 15 (*T0477a*), and (d) 16 (*T0501a*), with the start times aligned on ~0 s. The vertical black-dotted lines in the spectrograms indicate the time period of the waveforms below, given in a 5–9 Hz bandpass and with the same scale on all components. Shown are examples with minimum contamination of donks. LMST, Local Mean Solar Time; SF, super high frequency; SP, Short Period.
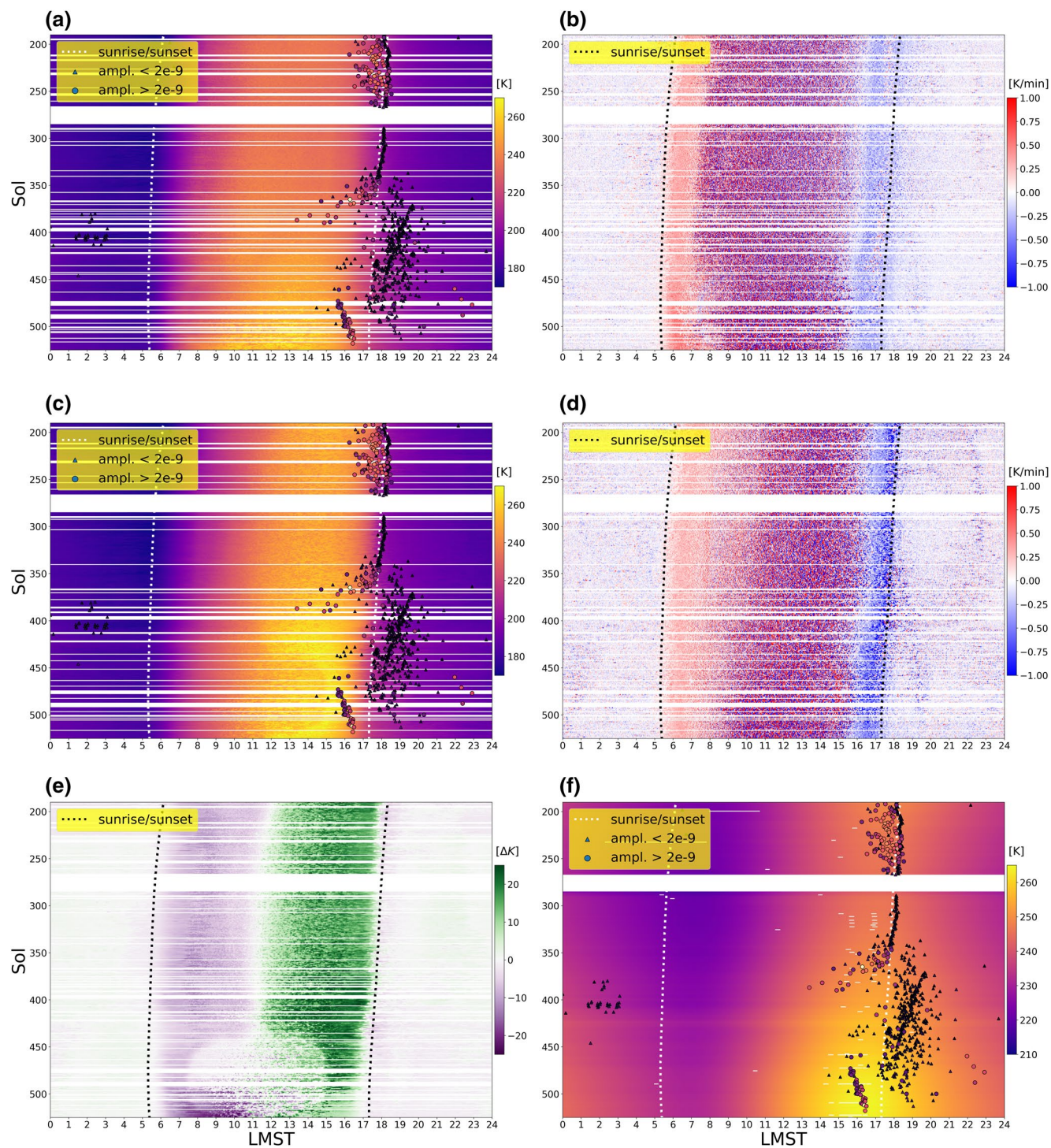
Figure A7. SF events and temperature from Sol 190 to 522: (a) atmospheric temperature - sensor 1 (channels 10.LKO, 10.VKO, 13.LKO), (b) rate of change of atm. temp. 1, (c) atm. temp.—sensor 2 (20.LKO, 20.VKO, 23.LKO), (d) rate of change of atm. temp. 2, (e) difference of both atm. temp. sensors (sensor 2—sensor 1) (f) scientific temperature (02.VKI, 03.VKI). Data gaps are marked in white. LMST, Local Mean Solar Time; SF, super high frequency.
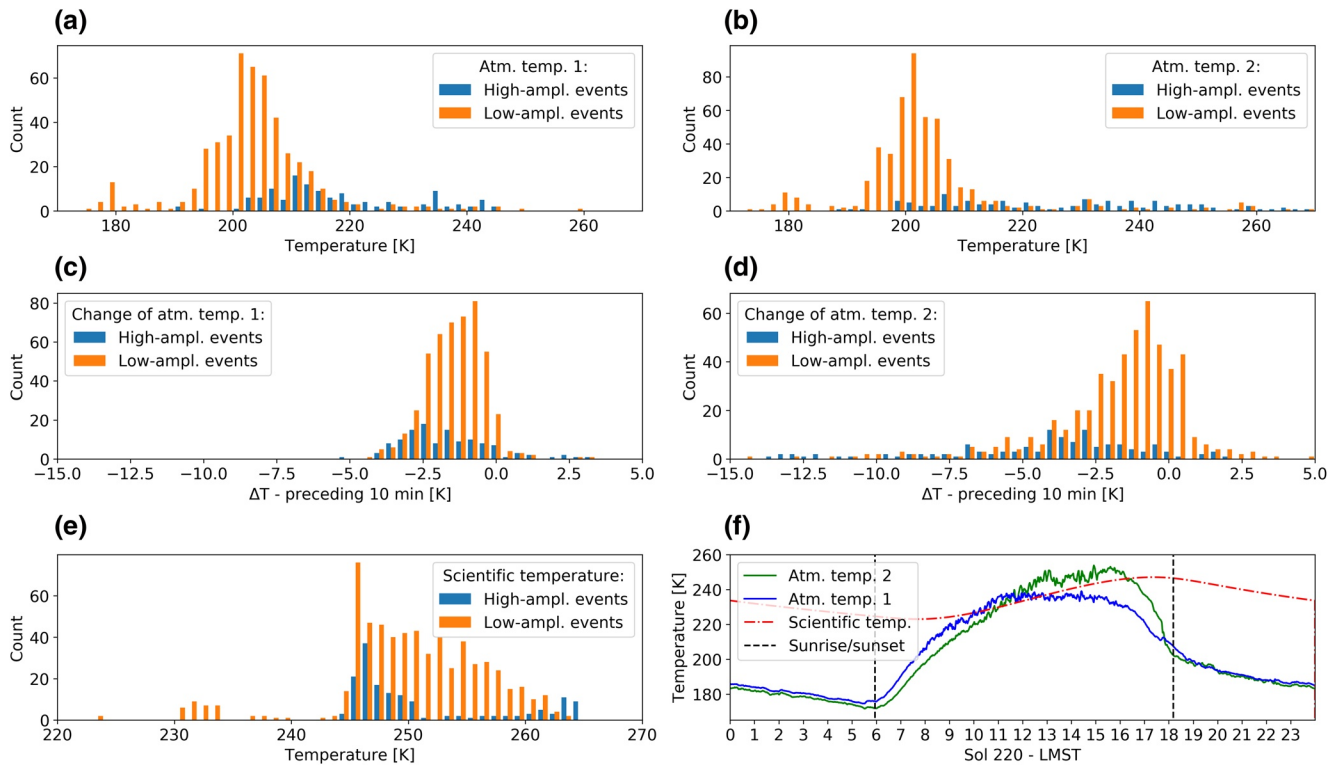
Figure A8. SF events and temperature: atmospheric temperature during high- and low amplitude events for (a) sensor 1 and (b) sensor 2; atmospheric temperature change in 10 min preceding the SF events for (c) sensor 1 and (d) sensor 2; (e) similar for scientific temperature inside WTS; the numbers include only events with available temperature measurements; (f) the atmospheric and scientific temperature curves for Sol 220. SF, super high frequency.

Data Availability Statement

The InSight seismic event catalog version 3 (InSight Marsquake Service, 2020) and waveform data are available from the IPGP Datacenter and IRIS-DMC (InSight Mars SEIS Data Service, 2019), as are previous catalog versions. Seismic waveforms are also available from NASA PDS (National Aeronautics and Space Administration Planetary Data System) (https://pds.nasa.gov/) (InSight Mars SEIS Data Service, 2019). The data collected during the Apollo missions are available through NSSDCA (NASA Space Science Data Coordinated Archive; https://nssdc.gsfc.nasa.gov/). The derived data including a list of the SF events with their characteristics, the similarity matrix and the stacked waveforms of each event family can be downloaded from 10.5281/zenodo.4049795 2020). The data were processed with ObsPy (Beyreuther et al., 2010), NumPy (Oliphant, 2006) and Scipy (Jones et al., 2001), and visualizations were created with Matplotlib (Hunter, 2007).

References

Banerdt, W. B., Smrekar, S. E., Banfield, D., Giardini, D., Golombek, M., Johnson, C. L., et al. (2020). Initial results from the InSight mission on Mars. *Nature Geoscience*, *13*(3), 183–189. http://dx.doi.org/10.1038/s41561-020-0544-y

Banfield, D., Spiga, A., Newman, C., Forget, F., Lemmon, M., Lorenz, R., et al. (2020). The atmosphere of Mars as observed by InSight. *Nature Geoscience*, *13*(3), 190–198. http://dx.doi.org/10.1038/s41561-020-0534-0

Beyreuther, M., Barsch, R., Krischer, L., Megies, T., Behr, Y., & Wassermann, J. (2010). ObsPy: A Python toolbox for seismology. *Seismological Research Letters*, *81*(3), 530–533. http://dx.doi.org/10.1785/gssrl.81.3.530

Bulow, R. C., Johnson, C. L., & Shearer, P. M. (2005). New events discovered in the Apollo lunar seismic data. *Journal of Geophysical Research*, *110*(E10). http://dx.doi.org/10.1029/2005je002414

Ceylan, S., Clinton, J. F., Giardini, D., Böse, M., Charalambous, C., van Driel, M., et al. (2020). Companion guide to the Marsquake catalog from InSight, sols 0-478: Data content and non-seismic events. *Physics of the Earth and Planetary Interiors*, 106597. http://dx.doi.org/10.1016/j.pepi.2020.106597

Clinton, J. F., Ceylan, S., van Driel, M., Giardini, D., Stähler, S. C., Böse, M., et al. (2020). The Marsquake catalogue from InSight, sols 0-478. *Physics of the Earth and Planetary Interiors*, 106595. http://dx.doi.org/10.1016/j.pepi.2020.10659

Clinton, J., Giardini, D., Böse, M., Ceylan, S., van Driel, M., Euchner, F., et al. (2018). The Marsquake service: Securing daily analysis of SEIS data and building the Martian seismicity catalogue for InSight. *Space Science Reviews*, *214*(8), 133. http://dx.doi.org/10.1007/s11214-018-0567-5

Compaire, N., Margerin, L., Garcia, R. F., Pinot, B., Calvet, M., Orhand-Mainsant, G., et al. (2020). Autocorrelation of the ground vibrations recorded by the SEIS-InSight seismometer on Mars. *Earth and Space Science Open Archive*, *25*. https://doi.org/10.1002/essoar.10503694.1

Cooper, M. R., Kovach, R. L., & Watkins, J. S. (1974). Lunar near-surface structure. *Reviews of Geophysics*, *12*(3), 291–308.

Dimech, J.-L., Knapmeyer-Endrun, B., Phillips, D., & Weber, R. C. (2017). Preliminary analysis of newly recovered Apollo 17 seismic data. *Results in Physics*, *7*, 4457–4458. http://dx.doi.org/10.1016/j.rinp.2017.11.029

Duennebier, F. (1976). Thermal movement of the regolith. *Lunar and Planetary Science Conference Proceedings*, *7*, 1073–1086.

Duennebier, F., & Sutton, G. H. (1974). Thermal moonquakes. *Journal of Geophysical Research*, *79*(29), 4351–4363.

Eppes, M., Willis, A., Molaro, J., Abernathy, S., & Zhou, B. (2015). Cracks in Martian boulders exhibit preferred orientations that point to solar-induced thermal stress. *Nature Communications*, *6*(1). http://dx.doi.org/10.1038/ncomms7712

Giardini, D., Lognonné, P., Banerdt, W. B., Pike, W. T., Christensen, U., Ceylan, S., et al. (2020). The seismicity of Mars. *Nature Geoscience*, *13*(3), 205–212. http://dx.doi.org/10.1038/s41561-020-0539-8

Gibbons, S. J., & Ringdal, F. (2006). The detection of low magnitude seismic events using array-based waveform correlation. *Geophysical Journal International*, *165*(1), 149–166. http://dx.doi.org/10.1111/j.1365-246x.2006.02865.x

Golombek, M., Kass, D., Williams, N., Warner, N., Daubar, I., Piqueux, S. et al. (2020a). Assessment of InSight landing site predictions. *Journal of Geophysical Research: Planets*, *125*(8). http://dx.doi.org/10.1029/2020je006502

Golombek, M., Williams, N., Warner, N. H., Parker, T., Williams, M. G., Daubar, I., et al. (2020b). Location and setting of the Mars InSight Lander, instruments, and landing site. *Earth and Space Science*, *7*(10), e2020EA001248. http://dx.doi.org/10.1029/2020ea001248

Hunter, J. D. (2007). Matplotlib: A 2D Graphics Environment. *Computing in Science & Engineering*, *9*(3), 90–95. http://dx.doi.org/10.1109/mcse.2007.55

InSight Mars SEIS Data Service. (2019a). *InSight SEIS Data Bundle. PDS Geosciences (GEO) Node*. https://doi.org/10.17189/1517570

InSight Mars SEIS Data Service. (2019b). *SEIS raw data, Insight Mission. IPGP, JPL, CNES, ETHZ, ICL, MPS, ISAE-Supaero, LPG, MFSC*. https://doi.org/10.18715/SEIS.INSIGHT.XB_2016

InSight Marsquake Service. (2020). *Mars seismic catalogue, InSight mission; V3 7/1/2020ETHZ, IPGP, JPL, ICL, ISAE-Supaero MPS, Univ Bristol. Dataset*. https://doi.org/10.12686/a8

Jones, E., Oliphant, T., Peterson, P., & Others (2001). *SciPy: Open source scientific tools for Python*. Retrieved from http://www.scipy.org/

Kovach, R. L., & Watkins, J. S. (1973). 10. Lunar seismic profiling experiment. Apollo 17: Preliminary Science Report, 330.

Lammlein, D. R., Latham, G. V., Dorman, J., Nakamura, Y., & Ewing, M. (1974). Lunar seismicity, structure, and tectonics. *Reviews of Geophysics*, *12*(1), 1–21.

Larose, E., Campillo, M., Khan, A., & Nakamura, Y. (2005). Lunar subsurface investigated from correlation of seismic noise. *Geophysical Research Letters*, *32*(16). http://dx.doi.org/10.1029/2005gl023518

Latham, G. V., Ewing, M., Press, F., Sutton, G., Dorman, J., & Nakamura, Y. (1970). *Apollo 11 passive seismic experiment*. MIT Press. https://doi.org/10.1126/science.167.3918.455

Lognonné, P., Banerdt, W. B., Giardini, D., Pike, W. T., Christensen, U., Laudet, P., et al. (2019). SEIS: Insight's seismic experiment for internal structure of Mars. *Space Science Reviews*, *215*(1), 12. http://dx.doi.org/10.1007/s11214-018-0574-6

Lognonné, P., Banerdt, W. B., Pike, W. T., Giardini, D., Christensen, U., Garcia, R. F., et al. (2020). Constraints on the shallow elastic and anelastic structure of Mars from InSight seismic data. *Nature Geoscience*, *13*(3), 213–220. http://dx.doi.org/10.1038/s41561-020-0536-y

Mimoun, D., Murdoch, N., Lognonné, P., Hurst, K., Pike, W. T., Hurley, J., et al. (2017). The noise model of the SEIS seismometer of the InSight mission to Mars. *Space Science Reviews*, *211*(1–4), 383–428. http://dx.doi.org/10.1007/s11214-017-0409-x

Harris, C. R., Jarrod Millman, K., van der Walt, S. J., Gommers, R., Virtanen, P., Cournapeau, D., et al. (2020). Array programming with NumPy. *Nature*, *585*(7825), 357–362. http://dx.doi.org/10.1038/s41586-020-2649-2

Schofield, J. T., Barnes, J. R., Crisp, D., Haberle, R. M., Larsen, S., Magalhães, J. A. et al. (1997). The Mars Pathfinder atmospheric structure investigation/meteorology (ASI/MET) experiment. *Science*, *278*(5344), 1752–1758. http://dx.doi.org/10.1126/science.278.5344.1752

Scholz, J.-R., Widmer-Schnidrig, R., Davis, P., Lognonné, P., Pinot, B., Garcia, R. F., et al. (2020). Detection, analysis, and removal of glitches from InSight's seismic data from Mars. *Earth and Space Science*, *7*(11), e2020EA001317. http://dx.doi.org/10.1029/2020ea001317

Sens-Schönfelder, C., & Larose, E. (2010). Lunar noise correlation, imaging and monitoring. *Earthquake Science*, *23*(5), 519–530. http://dx.doi.org/10.1007/s11589-010-0750-6

van Driel, M., Ceylan, S., Clinton, J. F., Giardini, D., Horleston, A., Margerin, L., et al. (2021). High-frequency seismic events on Mars observed by InSight. *Journal of Geophysical Research: Planets*, *126*, e2020JE006670. https://doi.org/10.1029/2020JE006670